

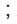





RESEARCH ARTICLE | APRIL 09 2021

## Time-resolved photoelectron imaging of complex resonances in molecular nitrogen **FREE**

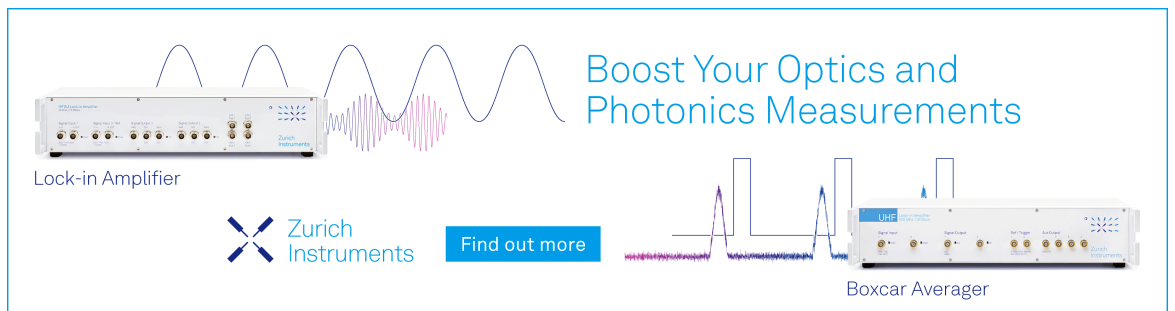
Mizuho Fushitani ; Stephen T. Pratt ; Daehyun You ; Shu Saito; Yu Luo; Kiyoshi Ueda ; Hikaru Fujise; Akiyoshi Hishikawa ; Heide Ibrahim ; François Légaré; Per Johnsson ; Jasper Peschel; Emma R. Simpson; Anna Olofsson; Johan Mauritsson ; Paolo Antonio Carpeggiani ; Praveen Kumar Maroju; Matteo Moiola; Dominik Ertel; Ronak Shah; Giuseppe Sansone ; Tamás Csizmadia; Mathieu Dumergue; N. G. Harshitha ; Sergei Kühn; Carlo Callegari ; Oksana Plekan ; Michele Di Fraia ; Miltcho B. Danailov ; Alexander Demidovich ; Luca Giannessi ; Lorenzo Raimondi; Marco Zangrando ; Giovanni De Ninno; Primož Rebernik Ribič ; Kevin C. Prince  



*J. Chem. Phys.* 154, 144305 (2021)

<https://doi.org/10.1063/5.0046577>

 CHORUS



Boost Your Optics and Photonics Measurements

Lock-in Amplifier

Zurich Instruments

Find out more

Boxcar Averager

# Time-resolved photoelectron imaging of complex resonances in molecular nitrogen

Cite as: J. Chem. Phys. 154, 144305 (2021); doi: 10.1063/5.0046577

Submitted: 4 February 2021 • Accepted: 19 March 2021 •

Published Online: 9 April 2021



Mizuho Fushitani,<sup>1</sup> Stephen T. Pratt,<sup>2,a)</sup> Daehyun You,<sup>3</sup> Shu Saito,<sup>3</sup> Yu Luo,<sup>3</sup> Kiyoshi Ueda,<sup>3,b)</sup> Hikaru Fujise,<sup>1</sup> Akiyoshi Hishikawa,<sup>1,4</sup> Heide Ibrahim,<sup>5</sup> François Légaré,<sup>5</sup> Per Johnsson,<sup>6</sup> Jasper Peschel,<sup>6</sup> Emma R. Simpson,<sup>6</sup> Anna Olofsson,<sup>6</sup> Johan Mauritsson,<sup>6</sup> Paolo Antonio Carpeggiani,<sup>7</sup> Praveen Kumar Maroju,<sup>8</sup> Matteo Moiola,<sup>8</sup> Dominik Ertel,<sup>8</sup> Ronak Shah,<sup>8</sup> Giuseppe Sansone,<sup>8</sup> Tamás Csizmadia,<sup>9</sup> Mathieu Dumergue,<sup>9</sup> N. G. Harshitha,<sup>9</sup> Sergei Kühn,<sup>9</sup> Carlo Callegari,<sup>10</sup> Oksana Plekan,<sup>10</sup> Michele Di Fraia,<sup>10</sup> Miltcho B. Danailov,<sup>10</sup> Alexander Demidovich,<sup>10</sup> Luca Giannessi,<sup>10,11</sup> Lorenzo Raimondi,<sup>10</sup> Marco Zangrando,<sup>10,12</sup> Giovanni De Ninno,<sup>10,13</sup> Primož Rebernik Ribič,<sup>10,13</sup> and Kevin C. Prince<sup>10,14,c)</sup>

## AFFILIATIONS

<sup>1</sup> Department of Chemistry, Nagoya University, Furo-cho, Chikusa, Nagoya, Aichi 464-8602, Japan

<sup>2</sup> Chemical Sciences and Engineering Division, Argonne National Laboratory, Lemont, Illinois 60439, USA

<sup>3</sup> Institute of Multidisciplinary Research for Advanced Materials, Tohoku University, Sendai, Miyagi 980-8577, Japan

<sup>4</sup> Research Center for Materials Science, Nagoya University, Furo-cho, Chikusa, Nagoya, Aichi 464-8602, Japan

<sup>5</sup> Institut National de la Recherche Scientifique, Centre Énergie Matériaux Télécommunications, Varennes, Québec J3X 1S2, Canada

<sup>6</sup> Lund University, Department of Physics, Lund, Sweden

<sup>7</sup> Technische Universität Wien, Institut für Photonik, Gußhausstraße 27-29, 1040 Wien, Austria

<sup>8</sup> Albert-Ludwigs-Universität, Stefan-Meier-Strasse 19, 79104 Freiburg, Germany

<sup>9</sup> ELI-ALPS, ELI-HU Non-Profit, Ltd., Wolfgang Sandner utca 3, Szeged H-6728, Hungary

<sup>10</sup> Elettra-Sincrotrone Trieste, SS 14, km 163.5, in Area Science Park, 34149 Basovizza, Trieste, Italy

<sup>11</sup> INFN, Laboratori Nazionali di Frascati, Via Enrico Fermi 54, 00044 Frascati (Roma), Italy

<sup>12</sup> IOM-CNR, SS 14, km 163.5, in Area Science Park, 34149 Basovizza, Trieste, Italy

<sup>13</sup> University of Nova Gorica, Vipavska 13, SI-5000 Nova Gorica, Slovenia

<sup>14</sup> Centre for Translational Atomaterials, and Department of Chemistry and Biotechnology, Swinburne University of Technology, Melbourne, Australia

<sup>a)</sup> E-mail: [stpratt@anl.gov](mailto:stpratt@anl.gov)

<sup>b)</sup> E-mail: [kiyoshi.ueda@tohoku.ac.jp](mailto:kiyoshi.ueda@tohoku.ac.jp)

<sup>c)</sup> Author to whom correspondence should be addressed: [prince@elettra.eu](mailto:prince@elettra.eu)

## ABSTRACT

We have used the FERMI free-electron laser to perform time-resolved photoelectron imaging experiments on a complex group of resonances near 15.38 eV in the absorption spectrum of molecular nitrogen, N<sub>2</sub>, under jet-cooled conditions. The new data complement and extend the earlier work of Fushitani *et al.* [Opt. Express 27, 19702–19711 (2019)], who recorded time-resolved photoelectron spectra for this same group of resonances. Time-dependent oscillations are observed in both the photoelectron yields and the photoelectron angular distributions, providing insight into the interactions among the resonant intermediate states. In addition, for most states, we observe an exponential decay of the photoelectron yield that depends on the ionic final state. This observation can be rationalized by the different lifetimes for the intermediate states contributing to a particular ionization channel. Although there are nine resonances within the group, we show that by detecting individual photoelectron final states and their angular dependence, we can identify and differentiate quantum pathways within this complex system.

Published under license by AIP Publishing. <https://doi.org/10.1063/5.0046577>

## I. INTRODUCTION

Molecular Rydberg states provide a rich environment for the investigation of intramolecular dynamics.<sup>1,2</sup> In particular, for intermediate values of the principal quantum number,  $n \sim 5-15$ , the electronic, vibrational, and rotational level spacings become comparable, leading to complex interactions that can provide insight into the flow of energy and angular momentum within the isolated molecule.<sup>1,2</sup> Such flows are an inherent part of chemical reactions, and their study can provide insight into the nature of chemical reactivity.

Spectroscopic studies have been particularly effective at revealing the coupling among molecular degrees of freedom, as well as the mechanisms that drive dynamical processes such as internal conversion, intersystem crossing, and dissociation.<sup>3,4</sup> Over the last few decades, time-domain studies using ultrafast lasers have provided a complementary perspective of these mechanisms.<sup>5-11</sup> More recently, ultrafast sources in the vacuum ultraviolet (VUV) have been developed based on high-harmonic generation, nonlinear frequency mixing, and free-electron lasers (FELs).<sup>12</sup> These sources allow direct excitation of the excited states of interest, and a number of new techniques have been developed to characterize the excited state structure and dynamics.<sup>6-11</sup> The present paper reports new ultrafast experiments using a combination of tunable, single-mode VUV light from the FERMI free-electron laser, a near-infrared (NIR) 795-nm (1.560 eV) probe laser, and photoelectron velocity map imaging to determine time-resolved photoelectron energy and angular distributions for a complex region of the spectrum of molecular nitrogen,  $N_2$ . This work builds on and extends a previous study of  $N_2$  by Fushitani *et al.*,<sup>13</sup> who recorded time-dependent photoelectron spectra in the same region.

The spectroscopy and dynamics of  $N_2$  have long been of interest due to their importance in understanding and modeling the Earth's upper atmosphere, the atmosphere of other planets and their moons, and interstellar chemistry.<sup>14,15</sup> The first ionization energy of  $N_2$  is at  $15.580\,726 \pm 0.000\,002$  eV,<sup>16</sup> and above  $\sim 12.6$  eV, the absorption spectrum rapidly becomes quite complex as a result of strong Rydberg–valence interactions, as well as interactions between the Rydberg series converging to the  $N_2^+ X^2\Sigma_g^+$  ground state and the low-lying  $A^2\Pi_u$  excited state.<sup>16-25</sup> In particular, long vibrational progressions are observed for the  $b^1\Pi_u$  and  $b'^1\Sigma_u^+$  valence states, as well as shorter progressions for the  $(X^2\Sigma_g^+)3p\pi c^1\Pi_u$ ,  $(X^2\Sigma_g^+)3p\pi c'^1\Sigma_u^+$ , and  $(A^2\Pi_u)3s\sigma o^1\Pi_u$  states. The interactions among these states were characterized in a classic set of papers by Lefebvre-Brion,<sup>17</sup> Dressler,<sup>18,19</sup> and Carroll and Collins.<sup>20</sup> At higher energy, transitions to higher members of the  $(X^2\Sigma_g^+)np\pi^1\Pi_u$ ,  $(X^2\Sigma_g^+)np\sigma^1\Sigma_u^+$ , and  $(A^2\Pi_u)ns\sigma^1\Pi_u$  series are observed, along with members of the  $(X^2\Sigma_g^+)nf$ ,  $(A^2\Pi_u)nd\sigma$ ,  $(A^2\Pi_u)nd\pi$ , and  $(A^2\Pi_u)nd\delta$  series.<sup>21-25</sup> Using a combination of very high-resolution absorption spectroscopy at room temperature and in supersonic beams and calculations based on multichannel quantum defect theory, Huber, Jungen, and their co-workers were able to provide a comprehensive analysis of the rotationally resolved spectra up to  $\sim 15.44$  eV.<sup>21,22,24,25</sup>

There have been a number of recent time-resolved photoelectron studies of the Rydberg states of  $N_2$ .<sup>13,26-28</sup> Zipp *et al.*<sup>26</sup> used ultrafast multiphoton excitation of the  $(X^2\Sigma_g^+)4f$  complex and a time-delayed ionization probe to study  $\ell$ -uncoupling of the Rydberg

electron from the rotating molecular frame. Here, the time dependence of the photoelectron angular distribution provided a signature of the uncoupled electron motion. Somewhat closer to the present experiments, Marceau *et al.*<sup>27</sup> used an ultrafast VUV source and time-resolved photoelectron spectroscopy to probe the region near 14 eV that includes the interacting  $b'^1\Sigma_u^+$ ,  $v' = 13$  valence band and the  $c_4'^1\Sigma_u^+$ ,  $v' = 4$  Rydberg band. The coherent excitation of the two bands leads to oscillations in the intensity of the selected photoelectron peaks, reflecting the energy splitting between the interacting states. In this example, the intermediate state was ionized by a two-photon process, and a resonant or near-resonant intermediate state was found to enhance the sensitivity to oscillations in selected ionization channels. In a study closely related to the present work, Trabs *et al.*<sup>29</sup> performed an ultrafast time-resolved photoelectron imaging study of the interacting Rydberg and valence states of NO. As discussed below, the similarities and differences between the present study and that earlier work help provide a context for the present findings.

Recently, Fushitani *et al.*<sup>13</sup> used high-harmonic generation to produce VUV light to excite  $N_2$  at  $\sim 15.380$  eV with a bandwidth of  $\sim 0.070$  eV and a time-delayed 800-nm (1.550 eV) probe to record

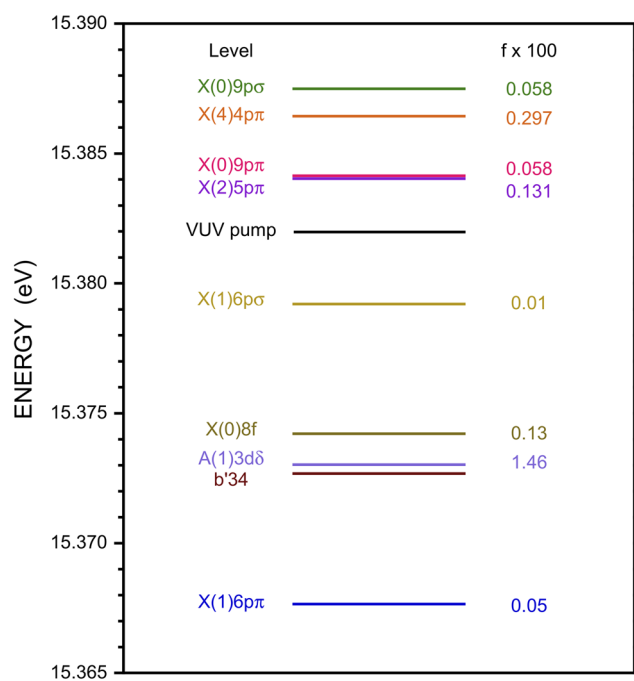


**FIG. 1.** An energy level diagram of the states in the region of the VUV pump photon energy. The right-hand side shows the oscillator strengths for each level extracted from Refs. 24 and 25. The Rydberg states are labeled  $\Lambda^+(v)n\ell\lambda$ , where  $\Lambda^+(=X^+, A^+)$  denotes the electronic state of the ion core,  $v$  denotes the vibrational quantum number,  $n$  and  $\ell$  denote the principal and orbital angular momentum quantum numbers for the Rydberg electron, and  $\lambda$  denotes the projection of  $\ell$  on the internuclear axis. The full width half maximum of the present VUV pulse was 0.023 eV, while that in the earlier experiments of Fushitani *et al.* was 0.070 eV. At lower energy, the next state corresponds to the  $X^+(0)8p\sigma$  state at 15.333 eV, while at higher energy, the next state corresponds to the  $X^+(2)5p\sigma$  state at 15.403 eV (see Ref. 25).

time-dependent photoelectron energy distributions with a resolution of  $\sim 94$  fs. The pump transition coherently excited both Rydberg and valence bands, and the photoelectron spectra showed time-dependent oscillations that provided information on the coupling between the Rydberg states, which are shown schematically in Fig. 1. In this figure and in what follows, we use the labeling scheme adopted by Fushitani *et al.*<sup>13</sup> Specifically, the Rydberg states are labeled  $\Lambda^+(v)n\ell\lambda$ , where  $\Lambda^+$  denotes the electronic state of the ion core,  $X^+$  or  $A^+$ ;  $v$  denotes the vibrational quantum number;  $n$  and  $\ell$  denote the principal and orbital angular momentum quantum numbers for the Rydberg electron; and  $\lambda$  denotes the projection of  $\ell$  on the internuclear axis.

In the present study, we extend the work of Fushitani *et al.*<sup>13</sup> by re-examining the same spectral region using photoelectron imaging to detect both the time-dependent photoelectron energy and angular distributions. The new experiments expand on the earlier work in two significant ways. First, the measurement of photoelectron angular distributions provides complementary information on the interaction among the pumped levels that is not revealed in the time-dependent ion yields or electron yields alone. Second, supersonic cooling of the sample in a molecular beam reduces the dephasing due to rotational effects in the room temperature sample of the earlier experiments. This cooling results in better defined coherent oscillations that can be followed over longer time delays.

In what follows, the details of the experiment are discussed in Sec. II. Next, the relevant portion of the absorption spectrum of  $N_2$  is described in more detail, and the basic principles and expectations for the time-dependent photoelectron energy and angular distributions are presented in Sec. III. The experimental results and their implications are presented in Sec. IV. This paper concludes with a discussion of potential extensions of the work, as well as of potential theoretical studies that could provide additional insight into the present findings.

## II. EXPERIMENT

The experiments were performed using FEL-1 at the FERMI free-electron laser facility.<sup>30</sup> The FERMI FEL is a seeded laser, and it was operated at a wavelength of 80.56 nm (15.390 eV) for the experiments described here. The FEL, beam-delivery system, and optical arrangement for the pump-probe experiments have been described previously.<sup>31–34</sup> The present experiments were performed using the velocity-map imaging photoelectron spectrometer in the low-density matter end station,<sup>35</sup> which has also been described previously.<sup>31,32</sup> Only the particular details of the present experiment are included here.

The FEL was operated at 50 Hz, and the VUV pulse duration was  $\sim 140$  fs full-width at half-maximum (FWHM), as measured by using sidebands in the NIR+VUV ionization of Xe. The pulse energy at the exit of the undulator was estimated to be  $\sim 25$   $\mu$ J and 5–6  $\mu$ J in the interaction region, assuming the calculated transmission of the photon transport optics.<sup>31</sup> The pulse energy monitors of FERMI are based on ionization of nitrogen and so do not measure the pulse energy below the ionization threshold. The PRESTO spectrometer<sup>33</sup> was used to measure the shot-by-shot spectra in this experiment, which were then integrated to give a value of intensity. The spectrometer was calibrated against gas ionization

detectors at shorter wavelength where these detectors function. This calibration was then corrected for the spectrometer efficiency as a function of wavelength. The bandwidth of the light was 0.023 eV (FWHM). The VUV light was focused with the active optics of the beamline to an approximately rectangular spot of dimensions  $94 \times 125$   $\mu$ m<sup>2</sup> by observing the spot on a fluorescent screen at the focus. The 795-nm (1.560 eV) probe pulse duration was 55 fs (FWHM), and the pulse energy was set to 21  $\mu$ J on the target for all of the present measurements. No significant multiphoton ionization was observed for pulse energies up to 500  $\mu$ J, and in the data, only one weak feature was observed and assigned to absorption of two IR photons. The probe beam was focused to a 40  $\mu$ m diameter spot (laser field intensity:  $1 \times 10^{13}$  W/cm<sup>2</sup>) overlapping the VUV beam. These pulse energies and focusing conditions resulted in a strong pump-probe signal while minimizing multiphoton effects from either beam alone. The VUV and NIR beams were both linearly polarized along the same axis, which was parallel to the plane of the imaging detector. This geometry facilitates the reconstruction of the photoelectron images.

The sample was introduced into the interaction region as a skimmed molecular beam produced by expanding 6 bars of pure  $N_2$  into the source chamber via a room-temperature Even-Lavie valve with an orifice of nominal diameter 100  $\mu$ m. Although we have no direct measurement of the rotational temperature of the sample, it can be estimated by using the data and analysis of Aoiz *et al.*<sup>36</sup> on similar expansions of  $N_2$ . With the present stagnation pressure and nozzle diameter, the sample translational and rotational temperatures are both expected to be below 10 K. The  $^{14}N$  nucleus has spin 1 so that  $^{14}N_2$  exists in two forms, with a population ratio of 2:1, and they do not interconvert readily under the present conditions.<sup>37</sup> The even:odd rotational levels of the  $X^1\Sigma_g^+$  ground state have 2:1 statistical weights.<sup>37</sup> At 10 K, the rotational distribution peaks at  $J'' = 0$ , and only 5% of the population is in levels with  $J'' = 2$ . This observation is important because it sets the timescale for rotational coherences that could be observed in the ionization process. In particular, excitation from  $J'' = 2$  could produce rotational coherences in the ionization process by interfering ionization pathways with intermediate states with  $J' = 1$  and 3. Using an approximate rotational constant,<sup>38</sup>  $B' = 2$  cm<sup>-1</sup>, the splitting between these two intermediate states is  $\sim 20$  cm<sup>-1</sup>, which would lead to coherences with oscillation periods of 1.7 ps. This timescale is just outside the range of the present experiments, but a fraction of a period may be observable as a slow modulation of the overall signal. Rotational coherences from  $J'' = 1$  would have even longer periods. Thus, the present discussion will focus on vibronic (or rovibronic) interactions coupling different electronic and vibrational levels.

The time-dependent photoelectron images were recorded by scanning the time delay between the VUV and NIR pulses from negative delays to 1.4 ps in 25 fs steps. Additional images were recorded every 3 laser shots in which the gas valve was not synchronized with the FEL pulse to allow the subtraction of background from the data. Four independent measurements of the time-dependent signal were summed to yield the final dataset. The data were reconstructed by using the BASEX approach of Dribinski *et al.*<sup>39</sup> The photoelectron energy scale was calibrated by using Xe as a calibration gas along with the known energies of the  $N_2$  photoelectron peaks obtained from the ionization energy<sup>16</sup> and vibrational constants of  $N_2^+$ .<sup>38</sup> The electric field in the interaction region of the imaging spectrometer

corresponds to  $\sim 10.5$  V/cm, which effectively reduces the ionization energy by  $\sim 19.8$  cm $^{-1}$ .<sup>40</sup>

For two-photon ionization in the weak-field electric-dipole approximation with linearly polarized light, the photoelectron angular distribution from a randomly oriented, non-chiral sample must take the form<sup>8,9</sup>

$$I(\Delta t, E_k, \theta) = \frac{\sigma(\Delta t, E_k)}{4\pi} [1 + \beta_2(\Delta t, E_k)P_2(\cos \theta) + \beta_4(\Delta t, E_k)P_4(\cos \theta)], \quad (1)$$

where  $\Delta t$  is the time delay,  $E_k$  is the photoelectron energy,  $\theta$  is the angle between the polarization axis and the electron velocity vector,  $\sigma$  is the cross section,  $\beta_i$  are the angular distribution parameters, and  $P_i(\cos \theta)$  are the Legendre polynomials.

In general,  $\beta_2$  and  $\beta_4$  values of zero correspond to isotropic distributions. Distributions for positive values of  $\beta_2$  and  $\beta_4$  are more strongly peaked along the polarization axis of the ionizing laser, while distributions for negative values are peaked more strongly perpendicular to this axis. The present analysis yields these angular distribution parameters as well as a quantity (which is referred to below as the electron or ionization yield) proportional to the cross section. These time-dependent quantities are the principal observables of the present experiments and analysis.

There are two sources of time-dependent behavior in the total ionization yield. First, there is a time dependence due to the intermediate state lifetime that results in the decay of the ionization yield with an increase in delay of the probe pulse. In principle, this time dependence is not expected to appear in the  $\beta_i$  parameters, which describe the shape of the angular distribution and are independent of the ionization yield; however, some exceptions to this are discussed below. The second time dependence is due to interference among alternative ionization pathways, leading to oscillations as a function of the pump-probe time delay. This dependence can appear in both the ionization yields and the angular distribution parameters.

The exponential decay of the electron yields for different photoelectron peaks can be fitted to determine decay constants and lifetimes. The oscillatory time-dependent waveforms can be Fourier transformed from the time domain to the frequency (or energy) domain to yield the splittings between intermediate states in the ionization process. To do this, the total electron yield was determined and, after suitable normalization, subtracted from each curve of photoelectron intensity. This time-dependent signal was extended by zero-padding (that is, adding a number of zeros) to extend the range of the trace, to make the number of time points a power of two, and to increase the density of interpolated points in the Fourier transform. As discussed below, each time trace was multiplied by a window function that strongly suppresses the contribution from negative time delays and from times when the VUV and NIR pulses overlap while retaining all of the signals for long time delays. For the present data, the combination of the number of time steps and the sampling rate limits the expected resolution of the Fourier transform to  $\sim 24$  cm $^{-1}$ . In what follows, we discuss both the exponential decay and the oscillatory behavior.

### III. BACKGROUND

#### A. Experimental considerations

As in the work of Fushitani *et al.*,<sup>13</sup> the present experiments are focused on a region of the single-photon excitation spectrum of N<sub>2</sub> between  $\sim 15.36$  and 15.40 eV. This is a complicated portion of the spectrum that includes transitions to nine different vibronic bands. Fortunately, Jungen *et al.*<sup>24</sup> performed a detailed analysis of these bands and the interactions among them by using a combination of rotationally resolved, jet-cooled absorption spectroscopy and theoretical calculations based on multichannel quantum defect theory. Figure 1 shows a schematic diagram of the vibronic bands in this region, along with the corresponding band oscillator strengths extracted by Huber *et al.*<sup>25</sup> The bands in this region are clustered into two groups. The A<sup>+</sup>(1)3dδ<sup>1</sup>Π<sub>u</sub>, X<sup>+</sup>(0)8f, and X<sup>+</sup>(1)6pπ bands form the low-energy group centered at  $\sim 15.373$  eV; the transition to the b'<sup>+</sup>1Σ<sub>u</sub><sup>+</sup>, v' = 34 valence band has also been predicted to lie near this energy but has not been observed.<sup>21,24</sup> The X<sup>+</sup>(4)4pπ, X<sup>+</sup>(2)5pπ, X<sup>+</sup>(0)9pπ, and X<sup>+</sup>(0)9pσ bands form the second group at  $\sim 15.386$  eV. The X<sup>+</sup>(1)6pσ band appears weakly midway between these two groups.

As discussed by Jungen *et al.*,<sup>24</sup> the vibronic states in this region are significantly mixed among each other through both homogeneous and heterogeneous interactions. Jungen *et al.*<sup>24</sup> indicated that most of the observed oscillator strength in this region is carried by the A<sup>+</sup>(1)3dδ<sup>1</sup>Π<sub>u</sub> level and that the other levels gain their intensity through interactions with this level. The interactions among all the states play an important role in the evolution of the time-dependent coherences and photoelectron spectra and asymmetry parameters described below.

In the previous work of Fushitani *et al.*,<sup>13</sup> the VUV light was centered at 15.38 eV with a bandwidth of 0.070 eV FWHM. This energy lies between the two groups of bands and the bandwidth allows the coherent excitation of the entire group of vibronic bands. In the present experiment, the photon energy was set by scanning the VUV wavelength and maximizing the total two-color signal for a delay of the NIR of 1.35 ps, yielding a VUV wavelength of 80.56 nm, or 15.39 eV with an estimated error of  $\pm 0.01$  eV. This error is determined by the precision of the seed wavelength, which was  $241.68 \pm 0.1$  nm. This energy is just on the high energy side of the higher energy group of bands. Alternatively, we can calibrate the photon energy based on published wavelengths and absorption cross sections. We calculated the predicted central wavelength by convoluting the absorption spectrum from Jungen *et al.*<sup>24</sup> with the VUV envelope to model the expected wavelength dependence of the total ionization signal in the absence of interference effects in the two-photon ionization signal. This approach yields an energy of 15.374 eV, but it neglects potential interference effects in the two-photon ionization signal, as well as intermediate-state lifetime effects due to the delayed probe pulse. The latter effects might influence the relative contributions of different intermediate states to the ionization signal and thus shift the measured intensity maximum. Averaging the results of the two approaches, we conclude that the center of the FEL pulse envelope is  $15.382 \pm 0.010$  eV.

While the 0.023 eV bandwidth of the FEL pulse is significantly smaller than that of the table-top source of Fushitani *et al.*,<sup>13</sup> it still allows the coherent excitation of all nine bands in this region.

A small change in the center energy would simply result in a different set of initial amplitudes for each of the vibronic levels. That is, each level would be weighted by its oscillator strength and its position on the intensity profile of the VUV pulse envelope. This uncertainty makes it difficult to perform detailed theoretical modeling of the observed time-dependent data.

## B. Theoretical considerations

In principle, the coherent excitation of nine different vibronic levels (not to mention the associated rotational levels) could result in a very complex time dependence for the observables. In the present experiments, however, the particular detection channel and observable act as filters that limit which states can contribute to the interference and oscillatory behavior. The nature of this filtering is different for the electron yields and the angular distribution parameters. While these ideas are known,<sup>27,41</sup> we briefly describe them in the context of the present experiments.

A model system with two intermediate states provides a framework for the present observations (Fushitani *et al.* 2019).<sup>13</sup> We consider four scenarios, which are illustrated schematically in Fig. 2. First, we consider coherent excitation of two intermediate states,  $|1\rangle$  and  $|2\rangle$ , that do not interact with each other [Fig. 2(a)]. The resultant wavepacket will be expressed as

$$\Psi(t) = a_1|1\rangle e^{-iE_1t/\hbar} + a_2|2\rangle e^{-iE_2t/\hbar}, \quad (2)$$

where the coefficients  $a_i$  ( $i = 1, 2$ ) are determined by the transition moments from the ground state and the intensity distribution of the excitation pulse. The energies of the intermediate states  $|i\rangle$  are given by  $E_i$ . If the two intermediate states are ionized to different (electronic or vibrational) ionic states such that the photoelectrons do not overlap in energy, the photoelectron intensity and angular distributions will be time independent.

Next, in Fig. 2(b), we consider the case in which the two intermediate levels  $|1\rangle$  and  $|2\rangle$  interact to form the eigenstates given by

$$\psi^+ = c_1|1\rangle + c_2|2\rangle \quad (3)$$

and

$$\psi^- = c_2|1\rangle - c_1|2\rangle. \quad (4)$$

The coherent excitation of these two levels results in a wavepacket described by

$$\begin{aligned} \Psi(t) &= a_+\psi^+ e^{-iE_+t/\hbar} + a_-\psi^- e^{-iE_-t/\hbar} \\ &= a_+(c_1|1\rangle + c_2|2\rangle)e^{-iE_+t/\hbar} + a_-(c_2|1\rangle - c_1|2\rangle)e^{-iE_-t/\hbar} \\ &= (a_+c_1e^{-iE_+t/\hbar} + a_-c_2e^{-iE_-t/\hbar})|1\rangle \\ &\quad + (a_+c_2e^{-iE_+t/\hbar} - a_-c_1e^{-iE_-t/\hbar})|2\rangle. \end{aligned} \quad (5)$$

In this case, even if the ionization of levels  $|1\rangle$  and  $|2\rangle$  leads to different final states, there will be two paths to each continuum, i.e.,

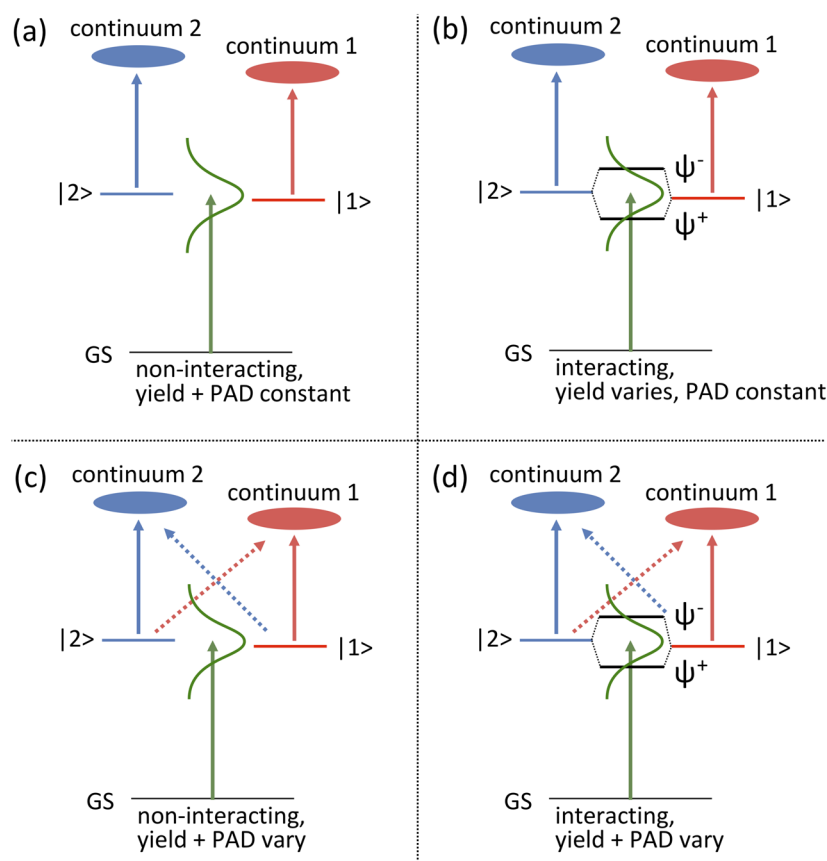


**FIG. 2.** Schematic illustration of the four cases considered for yields and photoelectron angular distributions (PADs). Green vertical arrows: FEL excitation; red or blue vertical arrows: NIR ionization. Horizontal lines represent the energies of states; GS is the ground state;  $|1\rangle$  and  $|2\rangle$  represent non-interacting excited states;  $\psi^\pm$  represent interacting excited states; and the blue and red ellipses represent the continuum states. The Gaussian curves represent the bandwidth of the FEL radiation. (a) Non-interacting intermediate states. (b) Interacting intermediate states. (c) Non-interacting intermediate states, ionization to the same continuum. (d) Interacting states, ionization to the same continuum.

via  $|+\rangle$  and  $|-\rangle$ . Since the two mixed states have different energies, their relative phases will vary with time, thus modifying the superposition coefficients in each channel and producing time-dependent oscillations in the photoelectron yields. However, because each final state is only populated by ionization of either  $|1\rangle$  or  $|2\rangle$ , the photoionization dynamics are always the same, and the angular distributions are still time independent, even though the yields in the two channels oscillate. An extension of this model to a system with three interacting states is described in the [supplementary material](#). That model shows how additional states result in additional oscillation frequencies.

In the third example, [Fig. 2\(c\)](#), we again consider non-interacting levels  $|1\rangle$  and  $|2\rangle$  as in [Eq. \(2\)](#) and [Fig. 2\(a\)](#) but with ionization from both levels into the same continuum (and the photoelectron peaks overlap in energy). Because there are then two pathways to the same final state and because  $|1\rangle$  and  $|2\rangle$  have different energies, the relative phase between the two paths is time dependent. This situation produces time-dependent ion yields, as well as time-dependent photoelectron angular distributions resulting from the time-dependent amplitudes of the interfering partial waves. This situation occurs in many experiments involving rotational coherences or hyperfine coherences in the intermediate state.<sup>42–44</sup>

Finally, we consider the case in which the intermediate states are mixed and ionization into the same ionization continuum is possible [[Fig. 2\(d\)](#)]. In this case, as in the previous one, both the electron yield and the angular distributions can show oscillations whose frequency is determined by the splitting between the two levels.

In principle, each pair of intermediate levels excited by the pump photon will produce an oscillation frequency in the electron yield and angular distributions if the right conditions are met. With nine intermediate levels (ignoring the rotational structure), this would result in 36 different frequencies. Here, however, two general propensities for the photoionization of Rydberg states result in a considerable simplification. First, the ion core of the Rydberg state generally acts as a spectator in the photoionization process, and it is preserved upon ionization. Second, the potential curves of Rydberg states are generally very similar to the corresponding ionic states, and the Franck–Condon factors for photoionization are thus often nearly diagonal.<sup>45</sup> If we assume that both assumptions are strictly valid, the number of possible interfering paths to each final state is greatly reduced. Furthermore, if most of the Rydberg state interactions are weak, a small number of oscillation frequencies are expected to dominate. Finally, we note that for closely spaced levels ( $\sim 24\text{ cm}^{-1}$ ) of the experiment, which is determined by the length of the time-delay scans.

While these propensities for the ionization step are expected to be generally applicable, there are several ways that they can break down. First, with respect to the preservation of the ion core upon photoionization, it is, in principle, possible for the ion core, rather than the Rydberg electron, to absorb the NIR photon. The corresponding photon energy is close to that of the  $\text{N}_2^+ A^2\Pi_u \leftarrow X^2\Sigma_g^+$  transition, particularly when one accounts for vibrational excitation.<sup>15,37</sup> Such processes are similar to “isolated core excitation” techniques used to extract information on the spectra of ions from Rydberg studies.<sup>40,46–48</sup> More generally, configuration interaction can result in ionizing transitions that look like two-electron, core-switching transitions. Second, because the potential

curves of the Rydberg states are not perfectly parallel with those of their corresponding ion cores (the Rydberg electron does affect the motion of the nuclei), the Franck–Condon factors for ionization will not be perfectly diagonal. Thus, ionizing transitions with  $\Delta v \neq 0$  will result in potential weaker interferences with both  $\Delta v = 0$  and  $\Delta v \neq 0$  transitions from other intermediate levels. Such  $\Delta v \neq 0$  transitions also allow the possible excitation of autoionizing resonances converging to the  $X^+(v > 5)$  and  $A^+(v > 1)$  levels at the two-photon energy. In principle, such resonances can decay into any of the open ionization continua, providing an additional pathway for interference that would likely lead to a very different photoelectron angular distribution from the direct ionization processes. Unfortunately, the autoionizing states of  $\text{N}_2$  with the required gerade symmetry have not been extensively explored.<sup>28,49</sup> The accurate theoretical treatment for each of these possibilities requires considerable care, and it is beyond the scope of the present work.

One additional mechanism can produce time-dependent angular distributions even without true interference effects. If there is one ionization process with an oscillating electron yield and a time independent angular distribution and a second ionization process that is time independent in both the yield and angular distribution, the angular distribution for two processes together will show a time dependence resulting from the varying contribution of the process with the time-dependent electron yield. For example, if there is a time-independent isotropic ionization signal ( $\beta_2 = \beta_4 = 0$ ) and a second ionization process with a time-dependent ion yield and a constant  $\beta_2 = 1$ , the observed  $\beta_2$  is the incoherent sum of the two processes and will follow the ion yield and oscillate between 1 and a value closer to 0. Such a mechanism has been proposed by Trabs *et al.*<sup>29</sup> to explain time-dependent angular distributions in two-photon ionization via Rydberg–valence mixed states in NO.

#### IV. RESULTS

[Figure 3\(a\)](#) shows an example of both the raw image and the reconstructed (inverted) image for two-color, VUV+NIR photoionization with a time delay of 950 fs. The reconstructed image allows the determination of both the angular distribution parameters,  $\beta_2$  and  $\beta_4$ , and integration over all angles allows the determination of the photoelectron yield as a function of the electron momentum or kinetic energy. [Figure 3\(b\)](#) shows a slice through the photoelectron yield data at a delay of 950 fs. This yield is similar to that observed previously by Fushitani *et al.*,<sup>13</sup> but some differences also exist. In particular, although the resolution of the present electron yield spectrum is not as high as that in the earlier study, it is clear that there are some differences in the relative intensities of different final state bands. For example, in [Fig. 3\(b\)](#), we conclude that the strong, lowest energy feature corresponds to the  $A^+(1)$  photoelectron band blended with the slightly higher energy  $X^+(5)$  band. This feature is considerably stronger than the corresponding feature in the early work.<sup>13</sup> The differences between the two spectra are most likely a result of the slightly different photon energies and bandwidths of the VUV pump beams, which will affect not only the intermediate state preparation but also the importance of any resonant feature (i.e., autoionizing levels) at the two-photon (VUV+NIR) energy in the continuum.

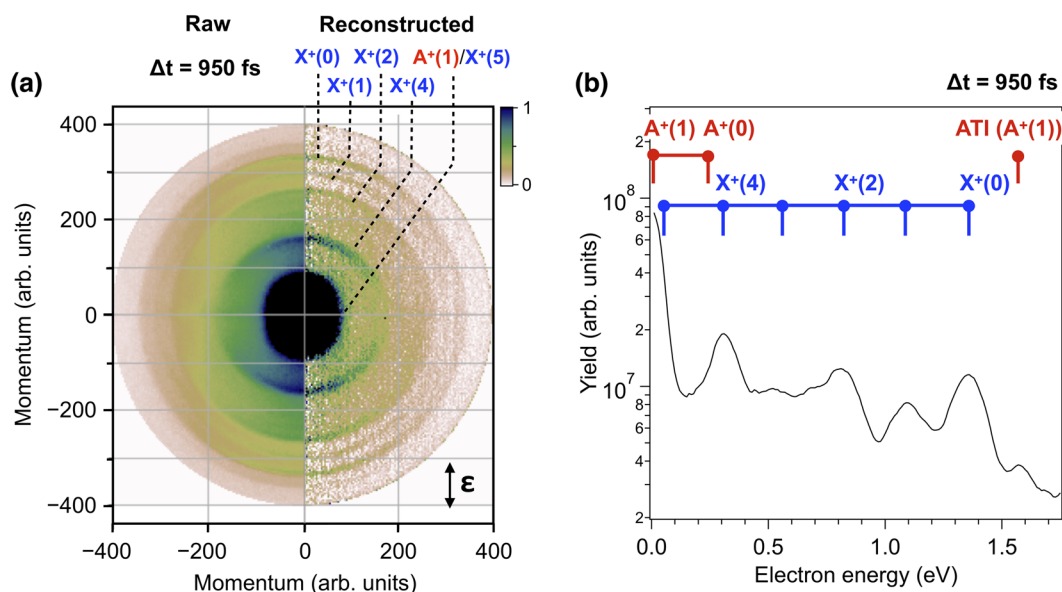


**FIG. 3.** (a) The raw (left) and reconstructed (right) photoelectron images following two-color, VUV+NIR ionization with a time delay of 950 fs. The  $\epsilon$  indicates the polarization direction of the VUV and NIR pulses, and the different final states are indicated in the reconstructed image. (b) The energy-calibrated photoelectron spectrum extracted from the reconstructed images by integrating over all angles.

Two other differences with the photoelectron spectrum of Fushitani *et al.*<sup>13</sup> deserve mention. First, a weak feature at 1.6 eV in the present data appears at  $t = 0$  and decays with an increase in time delay. This feature is attributed to the above-threshold ionization associated with the  $A^+(1)/X^+(5)$  band, that is, ionization of the intermediate states to populate the  $A^+(1)/X^+(5)$  levels by two (rather than one) 795 nm photons. Second, we have not determined the source of the shoulder on the low-kinetic-energy side of the  $X^+(2)$  peak.

By recording the image as a function of the delay between the VUV and NIR pulses, the time dependence of the photoelectron spectrum and angular distribution parameters can be determined. Figure 4 shows these photoelectron yields and  $\beta$  values as a function of the photoelectron energy and the time delay, as well as the corresponding Fourier transforms. Clear peaks are observed in the photoelectron yields along the energy axis, corresponding to the production of specific vibronic levels of the  $N_2^+$   $X^2\Sigma_g^+$  and  $A^2\Pi_u$  states. Along the time-delay axis, each of these peaks shows time-dependent behavior produced by the coherences prepared by the VUV pulse, as well as by the decay of the intermediate state population. Along the energy axes, the  $\beta_2$  and  $\beta_4$  plots show a structure similar to the electron yields, corresponding to the production of different vibronic levels of the ion. Along the delay axes, the  $\beta_2$  and  $\beta_4$  plots show similar oscillations to the electron yields, resulting from the interference among different ionization pathways.

In the Fourier transform analysis below, we consider only the  $N_2$  dynamics when the VUV and NIR pulses are not temporally overlapped. In this manner, the information is extracted from the  $N_2$  wavepackets without any influence of the strong NIR pulses.

When the pulses are temporally overlapped, the physical process is described by dressed states of the target, which are ionized non-sequentially. Such a treatment is beyond the scope of the present work. We note that there are some weak features in the photoelectron images at negative time delays to about  $-100$  fs, that is, when the IR pulse arrives before the FEL pulse. These features are assigned to non-sequential two-photon processes of the partially overlapping pulses. The full-width at half-maximum of the cross correlation of the two pulses is estimated to be  $\sim 150$  fs from the sidebands in the Xe photoelectron spectrum. Using the measured width of the IR pulse, 55 fs, and assuming that the cross correlation width is the sum in quadrature of the two pulse widths, we derived the estimated FEL pulse width of 140 fs.

Time traces for the electron yield and  $\beta$  parameters for each final state were obtained by integrating over the range of electron kinetic energies corresponding to that state at each time step. These traces are shown in Fig. 5. Some, but not all, of the electron yield curves show a smooth time-dependent decay reflecting the effective lifetime of the intermediate state(s) contributing to each photoelectron peak. Similar behavior was also noted by Fushitani *et al.*<sup>13</sup> Some of the  $\beta_i$  curves also show a similar smooth decay that is discussed in more detail below. In addition, most of the electron yield and  $\beta_i$  curves show an oscillatory behavior superimposed on the smooth decay. Perhaps the most surprising aspect of Fig. 5 is the relative simplicity of the oscillations observed in both the photoelectron yields and the angular distributions, especially given the potentially large number of ionization processes that could contribute to the signal. This observation clearly indicates that only a small number of ionization pathways dominate for each final state. In most cases, well-defined oscillations are observed in both the electron



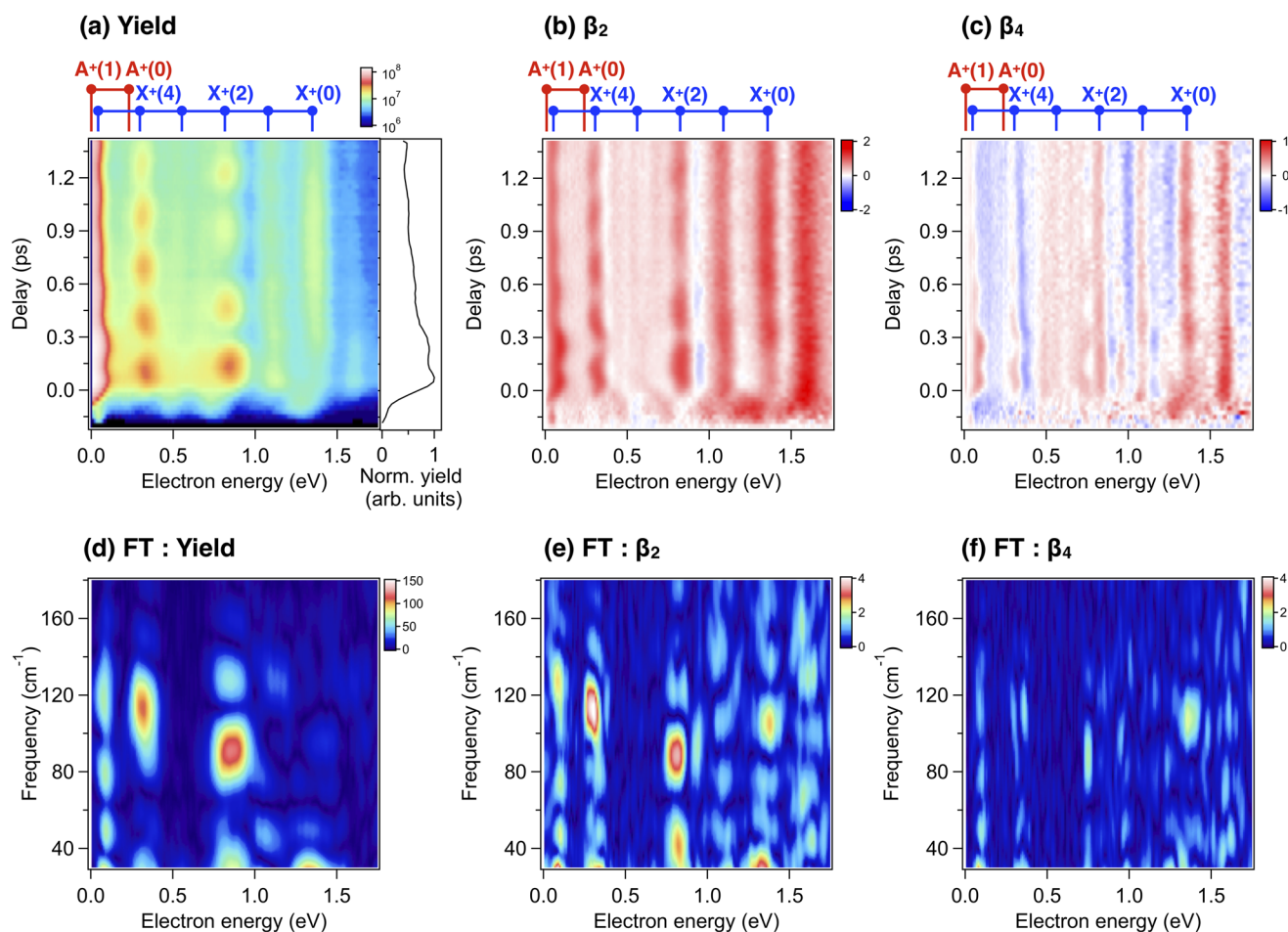


**FIG. 4.** (a) The photoelectron yield, (b) the  $\beta_2$  value, and (c) the  $\beta_4$  value for two-color, VUV+NIR ionization as a function of the photoelectron energy and the time delay between the VUV and NIR pulses. The trace to the right of (a) shows the total electron yield as a function of delay. The assignments of the final ionic levels are given at the top of each frame. [(d)–(f)] The Fourier transform as a function of electron kinetic energy for (d) the photoelectron yield, (e) the  $\beta_2$  value, and (f) the  $\beta_4$  value.

yields and  $\beta$  parameters. The oscillations observed in the electron yields are similar to those observed by Fushitani *et al.*,<sup>13,50</sup> but the present oscillations are better defined and more persistent than in the earlier work, an observation that most likely results from the lower rotational temperature here. In what follows, we first discuss the overall decay (or lack thereof) of the electron yield, and then, we discuss the oscillatory behavior of the electron yields and the  $\beta_i$  parameters.

## V. DISCUSSION

### A. Decay of the electron yield

In their earlier study,<sup>50</sup> Fushitani and Hishikawa fitted the decay of the  $X^+(2)$  photoelectron yield to a bi-exponential form with fast and slow time constants of 290(40) fs and 9(7) ps, respectively. In the present experiments, the limited range of time delays only allows the fitting of a single (fast) time constant. In particular, analysis of the present total electron yield for delays between

500 and 1250 fs gives a time constant of 450(50) fs. Fitting the present decay curves of individual photoelectron peaks is challenging. Even ignoring the oscillatory behavior, for the most part, the decays are not smooth exponentials, and the oscillations and phases of the oscillations add to the difficulty of extracting meaningful fits. Nevertheless, Table I shows the resulting time constants for both the full (0–1350 fs) traces and the time-delayed (200–1350 fs) portions when the VUV and NIR pulses do not overlap. Values with uncertainties greater than 100% are not included. In most instances, the time constants extracted from the full traces are shorter than those extracted from the delayed portions of the trace.

In principle, the different decay times for different photoelectron peaks are another aspect of the filtering associated with each detection channel. If, for example, a given final state is only produced by ionization via long-lived intermediate states, the decay constant of the photoelectron signal is expected to be much longer than if the final state is only reached via short-lived intermediate

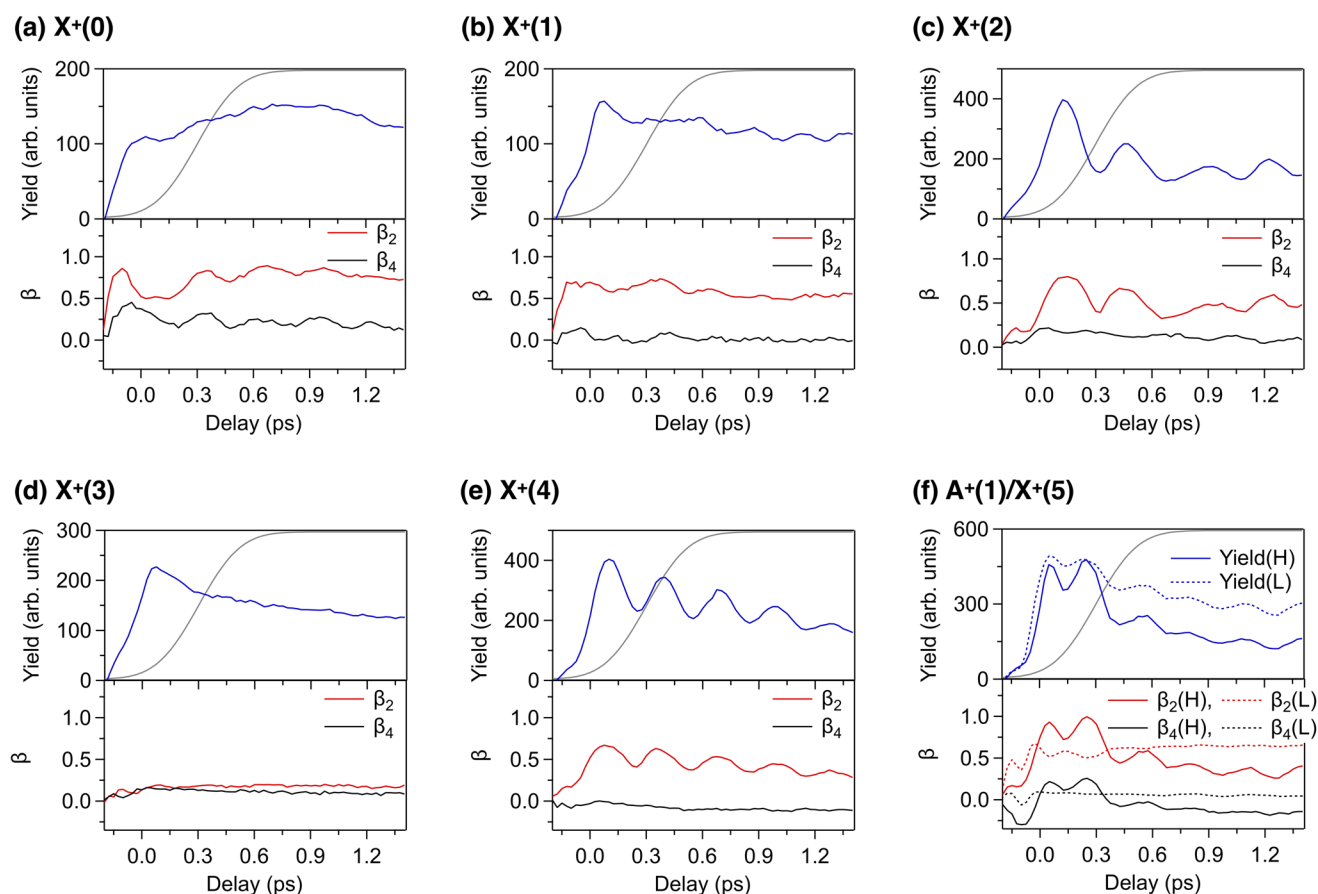


**FIG. 5.** Time-delay scans obtained by integrating the signal for the electron yield across individual photoelectron peaks (top, blue) and averaging the corresponding  $\beta_2$  and  $\beta_4$  values weighted by the electron yield across each peak for the following final states: (a)  $X^+(0)$ , (b)  $X^+(1)$ , (c)  $X^+(2)$ , (d)  $X^+(3)$ , (e)  $X^+(4)$ , and (f)  $A^+(1)/X^+(5)$ . In frame (f), the  $\beta_2$  and  $\beta_4$  values from the blended  $A^+(1)$  and  $X^+(5)$  peaks are separated into two components corresponding to the low and high energy sides of the photoelectron peak. The oscillation of the  $\beta_2$  values for these two components have the same frequency and opposite phases. The gray curve in the electron yield plots corresponds to the window function used in the Fourier transforms shown in Fig. 4.

states. In the energy region of interest, the largest contribution to the decay rate comes from the predissociation of the  $A^+(1)3d\delta^1\Pi_u$  state.<sup>24</sup> As can be seen in the work of Jungen *et al.*,<sup>24</sup> the corresponding widths in the high-resolution absorption spectrum are quite

**TABLE I.** Decay time constants for selected photoelectron peaks. Values in parentheses for the two traces are uncertainties.

Final state	Full trace (0–1350 fs)	Delayed trace <sup>a</sup> (200–1350 fs)
$X^+(0)$	No decay	No decay
$X^+(1)$	732(200)	...
$X^+(2)$	247(200)	...
$X^+(3)$	449(200)	834(86)
$X^+(4)$	871(200)	...
$A^+(1)/X^+(5)$	610(200)	266(39)

<sup>a</sup>Values are not reported for time constants with uncertainties greater than 100%.

large for the  $A^+(1)3d\delta^1\Pi_u$  state; the states that mix most strongly with the  $A^+(1)3d\delta^1\Pi_u$  state also have increased widths, while the states that mix only weakly with it have quite narrow widths. Recent high-resolution absorption spectra of jet-cooled  $N_2$  recorded using the VUV Fourier-transform spectrometer<sup>51</sup> at Synchrotron SOLEIL yield widths of  $\sim 2.2\text{ cm}^{-1}$  for transitions to individual rotational levels of the  $A^+(1)3d\delta^1\Pi_u$  state, but the lines are not fully resolved in those spectra. Those spectra also suggest that there may be a broader, very weak underlying continuum from the state responsible for the predissociation. In contrast, some of the lines in the high-resolution absorption spectra, such as those associated with transitions to the  $X^+(1)6p\pi$  and  $X^+(0)9p\pi$  states,<sup>51</sup> display resolution-limited widths of  $\sim 0.3\text{ cm}^{-1}$ . These two widths correspond to lifetimes of 2.4 ps and 17.6 ps, respectively.

The  $X^+(0)$  photoelectron intensity in Fig. 5(a) actually grows slightly with increasing delay before returning to approximately its initial value at the end of the time window. The lack of decay in this channel is not surprising because the transitions associated with

the three intermediate states with  $X^+(0)$  ion cores [i.e., the  $X^+(0)8f$ ,  $X^+(0)9p\pi$ , and  $X^+(0)9p\sigma$  states] that are expected to contribute most strongly to the  $X^+(0)$  photoelectron signal all have resolution-limited linewidths and thus much longer lifetimes than would be observable on the timescale of the present experiment.

All of the remaining photoelectron peaks have decay time constants of less than 1 ps. The shortest time constants are found for the  $A^+(1)/X^+(5)$  and  $X^+(2)$  peaks, corresponding to  $\sim 250$ – $270$  fs. This observation is consistent with the results of Fushitani and Hishikawa,<sup>50</sup> who found a decay time for the  $X^+(2)$  photoelectron signal of 290(40) fs. Note that the time constant determined from the full  $A^+(1)/X^+(5)$  trace is larger than that determined from the delayed trace as a result of a broad maximum in the trace near  $\Delta t = 0$  where the VUV and NIR pulses overlap, which is not fitted well by the exponential form. This behavior may also result from an interference oscillation with a long period outside the window of the experiment. The fast decay of the  $A^+(1)$  and  $X^+(2)$  intensities is not unexpected due to the fast predissociation of the  $A^+(1)3d\delta$  intermediate state and its relatively strong mixing with the  $X^+(2)5p\pi$  intermediate state.<sup>24</sup> The somewhat longer lifetimes for the other photoelectron peaks most likely reflect the weaker mixing of the relevant intermediate states with the predissociated  $A^+(1)3d\delta$  state.

The trends in the decay times for the different photoelectron peaks are consistent with expectations, and the decay time determined for the  $X^+(2)$  signal is consistent with the earlier measurements of Fushitani and Hishikawa. However, the decay times determined from the photoelectron signal seem surprisingly short compared to the expectations based on the linewidths in the high-resolution absorption measurements. For example, the decay time of 266 fs for the  $A^+(1)$  signal implies a width of  $\sim 19.8$   $\text{cm}^{-1}$ , which is significantly larger than the 2.2  $\text{cm}^{-1}$  widths observed in the absorption measurements. This discrepancy may reflect contributions from weak absorption directly to the state responsible for the predissociation of the  $A^+(1)$  state or contributions from higher rotational levels that predissociate faster as a result of a heterogeneous perturbation.<sup>4</sup>

In addition to the photoelectron yield curves, some of the  $\beta_i$  curves in Fig. 5 also show an overall decay (or growth) in the  $\beta_i$  values with time. Two possible explanations for this behavior can be proposed that are also based on the decay of the intermediate-state populations. First, if there are ionization pathways via two non-interacting intermediate states leading to the same continua [see Figs. 2(a) and 2(c)] and these two states have different lifetimes, the relative contribution of the two processes to the measured  $\beta_i$  will vary, ultimately reaching the value of the state with the longer lifetime. Alternatively, if there is an isotropic background contributing to the electron signal, it will produce a  $\beta_i = 0$  contribution to the overall signal. If the true signal has a significant positive or negative  $\beta_i$  value, the overall  $\beta_i$  value will decay from close to that value (depending on the relative magnitude of the background) at  $t = 0$  to  $\beta_i = 0$  at long times when the intermediate state has decayed.

## B. Oscillatory behavior of the electron yields and angular distributions

As discussed in Sec. III, of the nine vibronic levels in the bandwidth of the pump laser, three levels— $X^+(0)8f$ ,  $X^+(0)9p\pi$ , and

$X^+(0)9p\sigma$ —have  $X^+(0)$  cores. The propensity rules for ionization then suggest that ionization via all three levels will result in  $X^+(0)$ , and interference among the corresponding ionization pathways may produce oscillations in both the electron yields and the  $\beta_i$  parameters. This example is thus an illustration of the fourth scheme discussed in Fig. 2(d). The term energies for the  $X^+(0)8f$ ,  $X^+(0)9p\pi$ , and  $X^+(0)9p\sigma$  levels are 123 991, 124 081.45, and 124 108.28  $\text{cm}^{-1}$ , respectively,<sup>24</sup> leading to energy differences of 26.8, 90.5, and 117.3  $\text{cm}^{-1}$ , respectively. These differences will be modified somewhat when the rotational structure is considered. The  $X^+(0)9p\pi$  and  $X^+(0)9p\sigma$  levels interact with each other via the  $\ell$ -uncoupling operator.<sup>4</sup> In general, p-f interactions are expected to be weak, but all three levels may interact with the  $A^+(1)3d\delta^1\Pi_u$  level and thus can interact with each other in second order. In principle, the interaction with the  $A^+(1)3d\delta^1\Pi_u$  level could in itself produce oscillations in the electron yields in the  $X^+(0)$  photoelectron band, but it would not be expected to affect the  $\beta_i$  values because ionization from that level would primarily produce the  $A^+(1)$  state of the ion [see Fig. 2(b)].

The band oscillator strengths for the three  $X^+(0)$  bands have been determined by Huber *et al.*<sup>25</sup> The  $X^+(0)8f$  and  $X^+(0)9p\pi$  bands have a nearly equal oscillator strength of  $\sim 0.0013$ , while the  $X^+(0)9p\sigma$  value is  $\sim 0.00058$ . Two additional factors will affect the relative strengths of the three transitions from the ground state. First, the  $X^+(0)8f$  level gains essentially all of its intensity through interaction with  $A^+(0)3d\delta^1\Pi_u$ , and this interaction is strongest for the lowest rotational levels.<sup>24</sup> Because the experimental rotational temperature is expected to be quite low, the  $X^+(0)8f$  band may effectively be much stronger than expected relative to the  $X^+(0)9p\pi$  and  $X^+(0)9p\sigma$  bands. Second, the center wavelength of the VUV pulse envelope will also influence the relative importance of the different intermediate levels.

Figure 5(a) shows the time-dependent traces for the  $X^+(0)$  photoelectron band. The electron yield curve is relatively smooth, and it appears to show a single oscillation between 0.20 and 1.35 ps, starting low and reaching a maximum at  $\sim 0.675$  ps. This oscillation has a frequency of  $\sim 20$   $\text{cm}^{-1}$ , which is too low to be effectively captured with the present resolution in the Fourier transform. Nevertheless, the shape is reproduced reasonably well by a sine function with a frequency corresponding to the difference in term energies for  $X^+(0)9p\pi$  and  $X^+(0)9p\sigma$  levels (27.8  $\text{cm}^{-1}$ ),<sup>24</sup> and with a phase shift of  $\sim -2.54$  rad. The source of this phase shift has not been determined. Note that because the  $X^+(0)9p\pi$  and  $X^+(0)9p\sigma$  levels interact and because ionization of both states leads to the  $X^+(0)$  level of the ion [i.e., the case illustrated in Fig. 2(d)], the oscillations could be caused by the interactions between levels or by the interference between ionization pathways. The relatively small magnitude of the oscillation suggests that the overall effect is small.

In contrast to the  $X^+(0)$  electron yield, the  $X^+(0)$   $\beta_2$  and  $\beta_4$  values show significant oscillations at a higher frequency. Aside from the region in which the VUV and NIR pulses overlap, the  $\beta_2$  and  $\beta_4$  curves in Fig. 5(a) show similar oscillations that are approximately in phase, beginning at smaller values (more isotropic angular distributions), growing, and then oscillating with  $\beta_2$  ranging from  $\sim 0.4$  to 0.7 and  $\beta_4$  ranging from  $\sim 0.0$  to 0.25. For the  $X^+(0)$  final state, the Fourier transform of the  $\beta_2$  curve shows a broad feature centered at 105  $\text{cm}^{-1}$ , while the Fourier transform of the  $\beta_4$  curve shows a

strong feature at  $109\text{ cm}^{-1}$ . The similarities of the two curves suggest that the difference in the frequency simply reflects the large uncertainties in the measurements. The observed splittings are reasonably close to the splittings between the  $X^+(0)8f$  to  $X^+(0)9p\pi$  and  $X^+(0)8f$  to  $X^+(0)9p\sigma$  term energies ( $90.5$  and  $117.3\text{ cm}^{-1}$ , respectively), suggesting that ionization via all three states contributes to the  $X^+(0)$  photoelectron signal.

Figure 5(b) shows the time-dependent electron signal in the  $X^+(1)$  peak, along with those for the corresponding  $\beta_2$  and  $\beta_4$  parameters. The two potential intermediate levels with  $X^+(1)$  ion cores correspond to the  $X^+(1)6p\pi$  and  $X^+(1)6p\sigma$  levels, with term energies differing by  $93.2\text{ cm}^{-1}$ .<sup>24</sup> These levels are weakly mixed by the  $\ell$ -uncoupling operator.<sup>4</sup> Although the oscillations are not clearly visible Fig. 5(b), the Fourier transform of the electron yield shows a clear peak at  $128\text{ cm}^{-1}$ .

Figure 5(c) shows the time traces for the  $X^+(2)$  photoelectron signal and the corresponding  $\beta_i$  values. Here, both the yield and the  $\beta_2$  value show strongly modulated oscillations that reach a peak about  $75\text{ fs}$  after  $t = 0$ , while the  $\beta_4$  value is relatively constant. The  $X^+(2)5p\pi$  level is the only intermediate within the bandwidth of the VUV pulse with an  $X^+(2)$  core, but this level is mixed with the  $A^+(1)3d\delta^1\Pi_u$  level. The Fourier transforms for the  $X^+(2)$  yield and the  $\beta_2$  and  $\beta_4$  time traces show peaks at  $85\text{--}90\text{ cm}^{-1}$ . The  $\beta_2$  curve shows a second peak at  $41\text{ cm}^{-1}$ . For reference,<sup>24</sup> the  $A^+(1)3d\delta^1\Pi_u$  level lies  $88.8\text{ cm}^{-1}$  below the  $X^+(2)5p\pi$  level, in good agreement with the higher frequency feature. A peak at  $84\text{ cm}^{-1}$  was also observed in the corresponding Fourier transform of the photoelectron signal of the previous study.<sup>13</sup> A simple three-level model taking the  $X^+(4)4p\pi$  level into account in addition to the  $A^+(1)3d\delta$  and  $X^+(2)5p\pi$  levels quantitatively explains the appearance of the peak. The model also suggests that the relative phase of the wavefunctions can be inferred from the oscillation phase of the time-trace, as discussed for the two-level model<sup>13</sup> (see the [supplementary material](#)).

Figure 5(d) shows the time-dependent traces for the  $X^+(3)$  photoelectron peak. Here, there is no evidence for any significant oscillations in the electron yield or in the  $\beta_2$  and  $\beta_4$  parameters, and the electron yield for  $X^+(3)$  shows only the exponential decay described above. The  $X^+(3)$  photoelectron peak is quite small, which is not unexpected because there are no levels with the  $X^+(3)$  core within the bandwidth of the pump laser. The lack of oscillations suggests that a single weak process, for example, photoionization with  $\Delta v = \pm 1$ , leads to the observed signal.

Figure 5(e) shows the time-dependent traces for the  $X^+(4)$  photoelectron peak. The electron yield shows a clear oscillation that is out of phase with that of the  $A^+(1)$  peak.<sup>13</sup> As in the  $X^+(2)$  data, here the electron yield and  $\beta_2$  values show strong in-phase oscillations, with the first peak occurring at  $\sim 50\text{ fs}$  after  $t = 0$ . The corresponding  $\beta_4$  curve is again quite flat. The  $X^+(4)4p\pi$  level is the only intermediate with an  $X^+(4)$  core within the VUV bandwidth, but, as discussed by Jungen *et al.*,<sup>24</sup> the  $X^+(4)4p\pi$  level interacts with the  $A^+(1)3d\delta^1\Pi_u$  level as well, which has a term energy that is  $108.2\text{ cm}^{-1}$  lower. This value is in good agreement with the Fourier transforms of the time traces, which yield a strong peak at  $111\text{--}113\text{ cm}^{-1}$ . This interaction would not explain the oscillations in  $\beta_2$  unless photoionization of the  $A^+(1)3d\delta^1\Pi_u$  level also populated the  $X^+(4)$  state of the ion. One way in which this would be possible involves the autoionization mechanism discussed in more detail below.

The lowest energy band in the photoelectron energy spectrum of Fig. 3(b) is assigned to the unresolved  $X^+(5)$  and  $A^+(1)$  bands in the order of decreasing photoelectron energy. The two bands appear to have comparable intensities, but we note that the  $A^+(1)$  band was much stronger than the  $X^+(5)$  band in the earlier study by Fushitani *et al.*<sup>13</sup> As discussed in Sec. IV, this difference may result from small differences in the pump wavelength and two-photon energy in the two experiments. Although the  $A^+(1)3d\delta^1\Pi_u$  level lies within the pump bandwidth, there are no levels with  $X^+(5)$  ion cores in this neighborhood. This observation suggests that the stronger  $X^+(5)$  signal in the present experiment may result from the autoionization of resonances lying at the two-photon energy because the importance of such processes could depend strongly on the pump wavelength. Vibrational autoionization of Rydberg series converging to  $X^+(\geq 6)$  is expected to preferentially populate the  $N_2^+ X^+(5)$  level as a result of the vibrational propensity rule.<sup>52</sup> Electronic autoionization of Rydberg states converging to  $A^+(\geq 2)$  to populate  $X^+(\leq 6)$  levels is expected to be faster than vibrational autoionization of the same states to populate  $A^+(\leq 2)$  levels. The former process is expected to populate a range of  $X^+(v)$  levels, while the latter is expected to preferentially populate  $A^+(1)$ .

Figure 5(f) shows the time traces for these two components of the low-energy peak. We have integrated over the low- and high-energy regions of the band, and we avoided the region near the center where both components are contributing to the signal. The electron yields show similar time dependences, peaking at  $t = 0$  and displaying regular oscillations. The two  $\beta_2$  curves show oscillations with similar frequencies, but the comparison in Fig. 5(f) shows that the  $A^+(1)$  (lower energy) component is  $180^\circ$  out of phase with the  $X^+(5)$  (higher energy) component. The Fourier transforms of the  $\beta_2$  and  $\beta_4$  curves for the high-energy component show peaks at  $127$  and  $111\text{ cm}^{-1}$ , respectively, while those of the  $\beta$  curves for the low-energy component show no obvious peaks. The  $A^+(1)$  yield peaks at  $t = 0$  and oscillates  $\sim 180^\circ$  out of phase with the  $X^+(4)$  yield, as observed in the previous study. The Fourier transforms of both sets of electron yields show a peak at  $118\text{--}120\text{ cm}^{-1}$  for  $A^+(1)$  and  $113\text{ cm}^{-1}$  for  $X^+(4)$ . These values for the  $X^+(4)$  and  $A^+(1)$  photoelectron yields were both  $110\text{ cm}^{-1}$  in the earlier work of Fushitani *et al.*<sup>13</sup> This difference might reflect the somewhat different distribution of intermediate states prepared by the pump transition.

## VI. CONCLUSIONS

In the present work, time-resolved photoelectron energy and angular distributions were recorded following two-color, two-photon ionization of molecular nitrogen via a complex group of nine Rydberg and valence states centered around  $15.38\text{ eV}$  excitation energy. The most notable aspect of the present work is the remarkable simplification of the observed behavior that results from detecting the ionization process via a particular detection channel. For example, the ionization propensities for different intermediate states lead to the result that by monitoring the photoelectron signal for a particular final state, one can selectively enhance the detection of a specific ionization pathway or set of pathways. Similarly, by focusing on oscillations in the photoelectron angular distributions, one can selectively enhance only those pathways that produce the same continuum state. While such filtering has been discussed

previously,<sup>27,41</sup> the potential complexity of the present ionization process makes the observed simplicity of the results particularly striking.

For the present experiments, we have been able to build on the detailed analysis of the high-resolution absorption spectrum of N<sub>2</sub>,<sup>21,22,24,25</sup> which has allowed us to correlate the time-dependent behavior with the frequency domain data. The full power of the present approach will be revealed through the study of systems that are not nearly as well-characterized. Furthermore, while the present data clearly point to the important interactions and ionization pathways, realization of the full value of the approach will require some improvements in the experimental data. The first requirement is the need to extend the time-delay scans to much longer times. In particular, extending the delays to 15–20 ps would allow the detailed examination of the rotational structure and corresponding interactions, as well as of the nature of the electronic coherences.<sup>27,29,53</sup> Such data would allow a more detailed comparison with both high-resolution absorption measurements and the multichannel quantum defect analysis of Jungen *et al.*<sup>24</sup> Characterization of both the VUV and NIR wavelength dependence of the photoelectron data would also provide a more complete picture of the energetics and dynamics, particularly with respect to the role of autoionizing resonances and their influence on the time-dependent dynamics. Such states may ultimately prove valuable in controlling interferences and ionization dynamics. While there is considerable work to be done, the present study provides an important step in the application of time-resolved photoelectron imaging using FEL sources to the spectroscopy and dynamics of small molecules.

## SUPPLEMENTARY MATERIAL

See the [supplementary material](#) for a description of a three-level model for the time-resolved photoelectron intensity and for the photoelectron angular distributions. Figure S1 provides a graphical description of the Fourier transform procedure, and Figure S2 provides a summary of the results of the Fourier transforms.

## AUTHORS' CONTRIBUTIONS

All authors contributed equally to the data acquisition and treatment. This paper was drafted by S.T.P., refined in consultation with K.U. and K.C.P., and then circulated to all authors who contributed comments and constructive criticism.

## ACKNOWLEDGMENTS

We would like to thank the staff of the FERMI facility for their technical support and for ensuring the smooth operation of the experiments. S.T.P. was supported by the U.S. Department of Energy, Office of Science, Office of Basic Energy Sciences, Division of Chemical Sciences, Geosciences, and Biosciences under Contract No. DE-AC02-06CH11357. D.Y. acknowledges the Grant-in-Aid of the Tohoku University Institute for Promoting Graduate Degree Programs Division for Interdisciplinary Advanced Research and Education for support. K.U. acknowledges the Research Program of “Dynamic Alliance for Open Innovations Bridging Human, Environment and Materials” and the IMRAM project for support. H.I. and F.L. acknowledge funding from the NSERC and FRQNT. P.J. and J.P. acknowledge the support of the Swedish Research

Council and the Swedish Foundation for Strategic Research. J.M., A.O., and E.R.S. would like to acknowledge support from the Swedish Research Council (VR) and the Crafoord Foundation. J.M. and A.O. would like to acknowledge support from the Wallenberg Center for Quantum Technology (WACQT) funded by the Knut and Alice Wallenberg Foundation (Grant No. KAW 2017.0449). E.R.S. would like to acknowledge support from the Royal Physiographic Society of Lund. G.S., P.K.M., and M.M. acknowledge funding from the European Union's Horizon 2020 research and innovation program under Marie Skłodowska-Curie Grant Agreement No. 641789 MEDEA. G.S., D.E., and R.S. acknowledge funding from the Deutsche Forschungsgemeinschaft (DFG) [IRTG CoCo (2079) and QUTIF SA 3470/2]. The ELI-ALPS project (No. GINOP-2.3.6-15-2015-00001) was supported by the European Union and co-financed by the European Regional Development Fund. M.F. and A.H. acknowledge support from the Cooperative Research Program of “Network Joint Research Center for Materials and Devices” (Grant No. 20191083).

## DATA AVAILABILITY

The data that support the findings of this study are available from the corresponding author upon reasonable request.

## REFERENCES

- <sup>1</sup> *Molecular Rydberg Dynamics*, edited by M. S. Child (Imperial College Press, London, 1997).
- <sup>2</sup> M. S. Child, *Theory of Molecular Rydberg States* (Cambridge University Press, Cambridge, UK, 2011).
- <sup>3</sup> *Molecular Applications of Quantum Defect Theory*, edited by C. Jungen (Institute of Physics, Philadelphia, 1996).
- <sup>4</sup> H. Lefebvre-Brion and R. W. Field, *Spectra and Dynamics of Diatomic Molecules* (Elsevier, Amsterdam, 2004).
- <sup>5</sup> A. H. Zewail, “Femtochemistry: Atomic-scale dynamics of the molecular bond,” *J. Phys. Chem. A* **104**, 5660–5694 (2000).
- <sup>6</sup> T. Seideman, “Time-resolved photoelectron angular distributions: Concepts, applications, and directions,” *Annu. Rev. Phys. Chem.* **53**, 41–65 (2002).
- <sup>7</sup> A. Stolow, A. E. Bragg, and D. M. Neumark, “Femtosecond time-resolved photoelectron spectroscopy,” *Chem. Rev.* **104**, 1719 (2004).
- <sup>8</sup> T. Suzuki, “Femtosecond time-resolved imaging,” *Annu. Rev. Phys. Chem.* **57**, 555–592 (2006).
- <sup>9</sup> A. Stolow and J. G. Underwood, “Time-resolved photoelectron spectroscopy of nonadiabatic dynamics in polyatomic molecules,” *Adv. Chem. Phys.* **139**, 497–583 (2008).
- <sup>10</sup> K. L. Reid, “Photoelectron angular distributions,” *Annu. Rev. Phys. Chem.* **54**, 397–424 (2003).
- <sup>11</sup> K. L. Reid, “Photoelectron angular distributions: Developments in applications to isolated molecular systems,” *Mol. Phys.* **110**, 131–147 (2012).
- <sup>12</sup> L. Young, K. Ueda, M. Gühr, P. H. Bucksbaum, M. Simon, S. Mukamel, N. Rohringer, K. C. Prince, C. Masciovecchio, M. Meyer, A. Rudenko, D. Rolles, C. Bostedt, M. Fuchs, D. A. Reis, R. Santra, H. Kapteyn, M. Murnane, H. Ibrahim, F. Légaré, M. Vrakking, M. Isinger, D. Kroon, M. Gisselbrecht, A. L’Huillier, H. J. Wörner, and S. R. Leone, “Roadmap of ultrafast x-ray atomic and molecular physics,” *J. Phys. B: At., Mol. Opt. Phys.* **51**, 032003 (2018).
- <sup>13</sup> M. Fushitani, Y. Toida, F. Légaré, and A. Hishikawa, “Probing Rydberg–Rydberg interactions in N<sub>2</sub> by ultrafast EUV–NIR photoelectron spectroscopy,” *Opt. Express* **27**, 19702–19711 (2019).
- <sup>14</sup> R. P. Wayne, *Chemistry of Atmospheres*, 3rd ed. (Oxford University Press, Oxford, UK, 2000).
- <sup>15</sup> A. Lofthus and P. H. Krupenie, “The spectrum of molecular nitrogen,” *J. Phys. Chem. Ref. Data* **6**, 113–307 (1977).

- <sup>16</sup>R. Seiler, U. Hollenstein, G. M. Greetham, and F. Merkt, "Rydberg-state-resolved zero-kinetic-energy photoelectron spectroscopy," *Chem. Phys. Lett.* **346**, 201–208 (2001).
- <sup>17</sup>H. Lefebvre-Brion, "Theoretical study of homogeneous perturbations. II. Least-squares fitting method to obtain 'deperturbed' crossing Morse curves. Application to the perturbed  $^1\Sigma_u^+$  states of  $N_2$ ," *Can. J. Phys.* **47**, 541–545 (1969).
- <sup>18</sup>K. Dressler, "The lowest valence and Rydberg states in the dipole-allowed absorption spectrum of nitrogen. A survey of their interactions," *Can. J. Phys.* **47**, 546–562 (1969).
- <sup>19</sup>D. Stahel, M. Leoni, and K. Dressler, "Nonadiabatic representations of the  $^1\Sigma_u^+$  and  $^1\Pi_u$  states of the  $N_2$  molecule," *J. Chem. Phys.* **79**, 2541–2558 (1983).
- <sup>20</sup>P. K. Carroll and C. P. Collins, "High resolution absorption studies of the  $b^1\Pi_u \leftarrow X^1\Sigma_g^+$  system of nitrogen," *Can. J. Phys.* **47**, 563–589 (1969).
- <sup>21</sup>K. P. Huber and C. Jungen, "High-resolution jet absorption study of nitrogen near 800 Å," *J. Chem. Phys.* **92**, 850–861 (1990).
- <sup>22</sup>K. P. Huber, C. Jungen, K. Yoshino, K. Ito, and G. Stark, "The  $f$  Rydberg series in the absorption spectrum of  $N_2$ ," *J. Chem. Phys.* **100**, 7957–7972 (1994).
- <sup>23</sup>M. Sommavilla, U. Hollenstein, G. M. Greetham, and F. Merkt, "High-resolution laser absorption spectroscopy in the extreme ultraviolet," *J. Phys. B: At., Mol. Opt. Phys.* **35**, 3901–3921 (2002).
- <sup>24</sup>C. Jungen, K. P. Huber, M. Jungen, and G. Stark, "The near-threshold absorption spectrum of  $N_2$ ," *J. Chem. Phys.* **118**, 4517–4538 (2003).
- <sup>25</sup>K. P. Huber, M.-C. Chan, G. Stark, K. Ito, and T. Matsui, " $N_2$  band oscillator strengths at near-threshold energies," *J. Chem. Phys.* **131**, 084301 (2009).
- <sup>26</sup>L. J. Zipp, A. Natan, and P. H. Bucksbaum, "Imaging the breakdown of molecular-frame dynamics through rotational uncoupling," *Phys. Rev. A* **95**, 061403(R) (2017).
- <sup>27</sup>C. Marceau, V. Makhija, P. Peng, M. Hervé, P. B. Corkum, A. Y. Naumov, A. Stolow, and D. M. Villeneuve, "Non-Born–Oppenheimer electronic wave packet in molecular nitrogen at 14 eV probed by time-resolved photoelectron spectroscopy," *Phys. Rev. A* **99**, 023426 (2019).
- <sup>28</sup>A. Moise, K. C. Prince, and R. Richter, "Time-resolved study of excited states of  $N_2$  near its first ionization threshold," *J. Chem. Phys.* **134**, 114312 (2011).
- <sup>29</sup>P. Trabs, F. Buchner, M. Ghotbi, A. Lübcke, H.-H. Ritze, M. J. J. Vrakking, and A. Rouzée, "Time-, angle- and kinetic-energy-resolved photoelectron spectroscopy of highly excited states of  $NO$ ," *J. Phys. B: At., Mol. Opt. Phys.* **47**, 124016 (2014).
- <sup>30</sup>E. Allaria, L. Badano, S. Bassanese, F. Capotondi, D. Castronovo, P. Cinquegrana, M. B. Danailov, G. D'Auria, A. Demidovich, R. De Monte, G. De Ninno, S. Di Mitri, B. Diviacco, W. M. Fawley, M. Ferianis, E. Ferrari, G. Gaio, D. Gauthier, L. Giannessi, F. Iazzourene, G. Kurdi, N. Mahne, I. Nikolov, F. Parmigiani, G. Penco, L. Raimondi, P. Rebernik, F. Rossi, E. Roussel, C. Scafuri, C. Serpico, P. Sigalotti, C. Spezzani, M. Svandrik, C. Svetina, M. Trivó, M. Veronese, D. Zangrando, and M. Zangrando, "The FERMI free-electron lasers," *J. Synchrotron Radiat.* **22**, 485–491 (2015).
- <sup>31</sup>C. Svetina, C. Grazioli, N. Mahne, L. Raimondi, C. Fava, M. Zangrando, S. Gerusina, M. Alagia, L. Avaldi, G. Cautero, M. de Simone, M. Devetta, M. Di Fraia, M. Drabbel, V. Feyrer, P. Finetti, R. Katzy, A. Kivimäki, V. Lyamayev, T. Mazza, A. Moise, T. Möller, P. O'Keeffe, Y. Ovcharenko, P. Piseri, O. Plekan, K. C. Prince, R. Sergio, F. Stienkemeier, S. Stranges, M. Coreno, and C. Callegari, "The low density matter (LDM) beamline at FERMI: Optical layout and first commissioning," *J. Synchrotron Radiat.* **22**, 538–543 (2015).
- <sup>32</sup>V. Lyamayev, Y. Ovcharenko, R. Katzy, M. Devetta, L. Bruder, A. LaForge, M. Mudrich, U. Person, F. Stienkemeier, M. Krikunova, T. Möller, P. Piseri, L. Avaldi, M. Coreno, P. O'Keeffe, P. Bolognesi, M. Alagia, A. Kivimäki, M. Di Fraia, N. B. Brauer, M. Drabbel, T. Mazza, S. Stranges, P. Finetti, C. Grazioli, O. Plekan, R. Richter, K. C. Prince, and C. Callegari, "A modular end-station for atomic, molecular, and cluster science at the low density matter beamline of FERMI@Elettra," *J. Phys. B: At., Mol. Opt. Phys.* **46**, 1–8 (2013).
- <sup>33</sup>C. Svetina, D. Cocco, N. Mahne, L. Raimondi, E. Ferrari, and M. Zangrando, "PRESTO, the on-line photon energy spectrometer at FERMI: Design, features and commissioning results," *J. Synchrotron Radiat.* **23**, 35–42 (2016).
- <sup>34</sup>P. Finetti, A. Demidovich, O. Plekan, M. D. Fraia, R. Cucini, C. Callegari, P. Cinquegrana, P. Sigalotti, R. Ivanov, M. B. Danailov, C. Fava, G. De Ninno, M. Coreno, C. Grazioli, R. Feifel, R. J. Squibb, T. Mazza, M. Meyer, and K. C. Prince, "Optical setup for two-colour experiments at the low-density matter beamline of FERMI," *J. Opt.* **19**, 114010 (2017).
- <sup>35</sup>P. O'Keeffe, V. Feyrer, P. Bolognesi, M. Coreno, C. Callegari, G. Cautero, A. Moise, K. C. Prince, R. Richter, R. Sergio, M. Alagia, M. de Simone, A. Kivimäki, M. Devetta, T. Mazza, P. Piseri, V. Lyamayev, R. Katzy, F. Stienkemeier, Y. Ovcharenko, T. Möller, and L. Avaldi, "A velocity map imaging apparatus for gas phase studies at FERMI@Elettra," *Nucl. Instrum. Methods Phys. Res., Sect. B* **284**, 69–73 (2012).
- <sup>36</sup>F. J. Aoz, T. Díez-Rojo, V. J. Herrero, B. Martínez-Haya, M. Menéndez, P. Quintana, L. Ramonat, I. Tanarro, and E. Verdasco, "Low-temperature rotational relaxation of  $N_2$  studied with resonance-enhanced multiphoton ionization," *J. Phys. Chem. A* **103**, 823–832 (1999).
- <sup>37</sup>G. Herzberg, *Spectra of Diatomic Molecules* (Van Nostrand Reinhold, New York, 1950).
- <sup>38</sup>K. P. Huber and G. Herzberg, *Constants of Diatomic Molecules* (Van Nostrand Reinhold, New York, 1979).
- <sup>39</sup>V. Dribinski, A. Ossadtchi, V. A. Mandelshtam, and H. Reisler, "Reconstruction of Abel-transformable images: The Gaussian basis-set expansion Abel transform method," *Rev. Sci. Instrum.* **73**, 2634–2642 (2002).
- <sup>40</sup>T. F. Gallagher, *Rydberg Atoms* (Cambridge University Press, Cambridge, 1994).
- <sup>41</sup>G. Wu, P. Hockett, and A. Stolow, "Time-resolved photoelectron spectroscopy: From wavepackets to observables," *Phys. Chem. Chem. Phys.* **13**, 18447–18467 (2011).
- <sup>42</sup>P. M. Felker, "Rotational coherence spectroscopy: Studies of the geometries of large gas-phase species by picosecond time-domain methods," *J. Phys. Chem.* **96**, 7844–7857 (1992).
- <sup>43</sup>K. L. Reid, S. P. Duxon, and M. Towrie, "Observation of time- and angle-resolved photoelectron flux from an optically prepared state of a molecule. Hyperfine depolarization in  $NO(A^2\Sigma^+)$ ," *Chem. Phys. Lett.* **228**, 351–356 (1994).
- <sup>44</sup>R. Forbes, V. Makhija, J. G. Underwood, A. Stolow, I. Wilkinson, P. Hockett, and R. Lausten, "Quantum-beat photoelectron-imaging spectroscopy of Xe in the VUV," *Phys. Rev. A* **97**, 063417 (2018).
- <sup>45</sup>S. T. Pratt, "Excited-state molecular photoionization dynamics," *Rep. Prog. Phys.* **58**, 821–883 (1995).
- <sup>46</sup>W. E. Cooke, T. F. Gallagher, S. A. Edelstein, and R. M. Hill, "Doubly excited autoionizing Rydberg states of Sr," *Phys. Rev. Lett.* **40**, 178 (1978).
- <sup>47</sup>D. P. Taylor, J. G. Goode, J. E. LeClaire, and P. M. Johnson, "Photoinduced Rydberg ionization spectroscopy," *J. Chem. Phys.* **103**, 6293–6295 (1995).
- <sup>48</sup>A. Sen and S. T. Pratt, "Double-resonance studies of electronically autoionizing states of molecular nitrogen," *Mol. Phys.* **117**, 2930–2940 (2019).
- <sup>49</sup>A. de Lange, R. Lang, W. van der Zande, and W. Ubachs, "Highly excited states of gerade symmetry in molecular nitrogen," *J. Chem. Phys.* **116**, 7893–7901 (2002).
- <sup>50</sup>M. Fushitani and A. Hishikawa, "Single-order laser high harmonics in XUV for ultrafast photoelectron spectroscopy of molecular wavepacket dynamics," *Struct. Dyn.* **3**, 062602 (2016).
- <sup>51</sup>N. de Oliveira, S. T. Pratt, B. Gans, U. Jacovella, S. Boyé-Péronne, K. Ito, D. Joyeux, and D. M. P. Holland, "The high-resolution photoabsorption spectrum of  $N_2$  in the vacuum ultraviolet" (unpublished) (2020).
- <sup>52</sup>R. S. Berry, "Ionization of molecules at low energies," *J. Chem. Phys.* **45**, 1228–1245 (1966).
- <sup>53</sup>V. Makhija, K. Veyrinas, A. E. Boguslavskiy, R. Forbes, I. Wilkinson, R. Lausten, S. P. Neville, S. T. Pratt, M. S. Schuurman, and A. Stolow, "Ultrafast molecular frame electronic coherences from lab frame scattering anisotropies," *J. Phys. B: At., Mol. Opt. Phys.* **53**, 114001 (2020).